

# Impedance Spectroscopy for Diagnosis of Photovoltaic Modules Under Outdoor Conditions

Rudy Alexis Guejia-Burbano , Giovanni Petrone , Senior Member, IEEE, and Michel Piliouguine 

**Abstract**—This work is aimed at detecting degradation phenomena on photovoltaic (PV) panels working under real outdoor conditions by using the impedance spectroscopy technique. The impedance is measured by leaving the PV panel in the real-operative status corresponding to the maximum power point without altering its power production. Since variations on the series resistance are associated with multiple degradation phenomena, this study seeks to estimate changes in this parameter using a dynamic model fitted to the experimental impedance measurements. An external resistor is added in series to the PV panel for emulating the degraded conditions. Hence, the PV panel impedance measurements are compared in nominal and degraded conditions. The results show that the dynamic model provides higher accuracy in comparison with the series resistance variation identified through the single-diode model, which is the most usual approach. Thus, it is demonstrated the feasibility of detecting degradation effects by using the dynamic model of PV panels working under outdoor conditions.

**Index Terms**—Degradation, diagnosis, impedance spectroscopy, outdoor conditions, photovoltaic (PV) module, series resistance.

## I. INTRODUCTION

THE large penetration of photovoltaic (PV) systems in the electrical distribution network leads to greater attention to the monitoring of the status of health of PV systems since their faults might have a relevant impact on the grid energy production [1]. Indeed, PV panels operating at outdoor conditions inevitably generate degradation processes due to multiple reasons, such operation in nonoptimal conditions (e.g., partial shading, hot spots), and environmental conditions. These processes gradually decrease the performance of the PV devices leading to the reduction in power production, lifetime, and money earnings. These undesirable effects support the importance of early detection for planning the minimization of such

outcomes [2]. Many studies on PV solar panel degradation are performed in laboratory, they have great validity, but only cover controlled conditions.

In contrast, outdoor implementations have to deal with arbitrary meteorological conditions meaning a true-operating environment. Those operating conditions generate challenges linked to the temperature, irradiance, wind, humidity, and other factors that impact the PV performance, giving great importance to outdoor research studies. They will confront and assess the PV panel to the true-operative conditions while producing power [3], [4].

The performance evaluation of PV panel is usually done through the single-diode model (SDM) that gives a tradeoff between acceptable accuracy and medium complexity. The key point of this model is the capability of reproducing the electrical  $I$ - $V$  curve of a PV source at the different operating conditions by using only a set of five parameters. The variations of such parameters are then associated to the environmental conditions and to the status of health of the PV panel [5], [6]. Among these parameters, the series resistance ( $R_s$ ) appears as a key parameter due to its straightforward relation with several degradation effects in PV devices. Sera et al. [7], [8] show that the series resistance is the main element that affects the fill factor. Here, degrading welding points and malfunctioning cells are linked to the variation in this parameter. Stein et al. [9] assume the series resistance as a representation of all contacts, series-connected cell layers, and wires. Therefore, a change in this element can be associated with corrosion and UV degradation. Deceglie et al. [10] consider the series resistance as an indicator of broken ribbons, broken solder bonds, and contact problems. Finally, in [11], the  $R_s$  is viewed as a representation of all signs correlated to the degradation processes. All authors show the relevance of this factor and propose different ways for calculating it utilizing the  $I$ - $V$  curve measurements, especially the points close to the open-voltage circuit. Although the SDM can reproduce correctly the static  $I$ - $V$  characteristic of a PV device, it cannot deal with its dynamic response, that requires an analysis in the frequency domain [12]. This analysis should provide additional information helping to better identify the degradation phenomena.

Table I summarizes the main information of different methods proposed in the literature for analyzing the PV dynamic response. The techniques are mainly devoted to the performance evaluation of PV cells for validating the PV manufacturing process, for studying physical phenomena occurring inside the cell, for identifying parameters of dynamic models, as well as

Manuscript received 14 March 2022; revised 26 April 2022; accepted 6 July 2022. Date of publication 10 August 2022; date of current version 28 November 2022. This work was supported in part by the Ministero dell'Istruzione, dell'Università e della Ricerca (Italy) under Grant PRIN2020-HOTSPHOT, Grant 2020LB9TBC, Grant PRIN2017-HEROGRIDS, and Grant 2017WA5ZT3\_003, in part by the Università degli Studi di Salerno [FARB funds], and in part by the Ministerio de Ciencia, Innovación y Universidades (Spain) under Grant RTI2018-095097-B-I0. (Corresponding author: Rudy Alexis Guejia-Burbano.)

The authors are with the Dipartimento di Ingegneria dell'Informazione ed Elettrica e Matematica Applicata/DIEM, University of Salerno, 84084 Fisciano, Italy (e-mail: rudy.guejia@correounivalle.edu.co; gpetrone@unisa.it; mpiliouguine@unisa.it).

Color versions of one or more figures in this article are available at <https://doi.org/10.1109/JPHOTOV.2022.3195003>.

Digital Object Identifier 10.1109/JPHOTOV.2022.3195003

TABLE I  
PRELIMINARY STUDIES THAT CHARACTERIZE SOLAR PV CELLS/MODULES

Characteristic	Reference												
	[15]	[16]	[17]	[18]	[19]	[20]	[21]	[13]	[22]	[23]	[14]	[24]	[25]
Testing Condition													
Dark	•	•					•	•	•	•	•		
Controlled $G$ and $T$	•	•	•	•	•	•	•	•					•
Outdoor conditions												•	
Technology													
sc-Si	•	•	•		•	•	•		•	•	•		
mc-Si				•				•	•			•	•
Technique													
Square wave signal	•												
Impedance Spectroscopy		•	•	•	•	•	•	•	•	•	•		
Reflectometry												•	•
Objective													
Physics							•						
Manufacturing							•						
Modeling	•	•	•	•	•	•							
Fault detection									•			•	•
Degradation analysis								•		•	•		
Frequency Range													
1Hz-30kHz	•												
1Hz-100kHz			•					•	•		•		
0.1Hz-100kHz				•									
1Hz-1MHz					•								
150Hz-200kHz						•							
42Hz-5MHz							•						
20Hz-100kHz										•			
0.01Hz-1MHz		•											
20Hz-200kHz													•
PV level													
Cell	•	•	•	•	•	•	•	•					•
Module/Array									•	•	•	•	

for the analysis of degradation and fault detection inside PV cells and modules. Usually the testing conditions refer to PV cells or modules operating in dark conditions or under controlled irradiance  $G$  and temperature  $T$ . Table I also shows the ranges of the stimulation frequency used for testing the PV cells and modules made with single-crystalline (sc-Si) and multicrystalline (mc-Si) silicon PV technologies.

Electrical impedance spectroscopy (EIS) methodology is a well-established technique to characterize electrochemical devices (e.g., batteries, fuel cells, supercap) in the frequency domain. EIS applied to PV systems is relatively new, but, despite it, good preliminary results have been reached for the last few years, especially for the diagnosis of degradation processes [13], [14]. One common limitation of these previous works is their on-field applicability, because they are under controlled conditions (irradiance and temperature) with single solar cells. Some of them have used small solar panels, but still in a laboratory environment.

This article mainly contributes to validate the using of the EIS methodology for commercial PV panels for detecting degradation effects under real-operating outdoor conditions. It means, there is no control over the environmental variables that continuously modify the PV panel operating point. Due to the strong sensibility of the PV panel impedance regarding the operating point, a method to correlate the measured impedance with the outdoor-operating condition is proposed. Hence, this work concentrates on performing the EIS methodology at the maximum power point (MPP) of the system since

its impedance spectrum exhibits a particular correlation with the PV current and voltage measured in MPP. Then, the measured impedance spectrum in MPP allowed for building an accurate identification of the series resistance ( $R_s$ ) degradation by using a proper PV small-signal dynamic model.

It is worth to note that other methods proposed in the literature commonly need to measure the whole  $I$ - $V$  curve or part of it to estimate  $R_s$  through static models, e.g., the SDM. Thus, the series resistance degradation is quantified through the difference of the  $R_s$  parameter at different conditions. These methods require to bias the system far from the MPP, the best operative condition, for measuring data occasionally or repetitively. As a consequence, energy and money losses could arise, besides negative impacts on the electronic system equipment due to the frequently changes in the operating conditions. On the contrary, the EIS methodology estimates the series resistance without changing the operating point, thus, still working in MPP. To the best of authors' knowledge, this is the first time that the series resistance degradation is estimated by using only the impedance spectrum measured at MPP.

Moreover, we must highlight that, the adoption of module-level and submodule-level power electronics is becoming more and more usual, especially for mitigating the impact of partial shading on the energy production of residential and small commercial PV systems [26]. Distributed power electronics assures a local monitoring and control, and gives the space for developing powerful on-field diagnostic techniques, e.g., based on the EIS method, that could help us to predict and maintain the PV status of health in a more effective way. The experimental results provided this article, even if still obtained through a lab equipment, demonstrate the potentiality of the technique for the on-board implementation in the near future.

The rest of this article is organized as follows. Section II describes the experimental platform: equipment and setups. The basic theory of the EIS dynamic models and the operative considerations for implementing the methodology on PV panels is also reported in Section II. In Section III, the experimental data are fitted to the dynamical PV model for finding the parameters values able to detect the series resistance degradation phenomenon. Finally, Section IV concludes this article.

## II. METHODOLOGY

### A. Experimental Platform Description

Fig. 1 presents the setup employed for characterizing a commercial sc-Si PV module placed on the roof of the Engineering Building of the University of Salerno (Italy). The main features of this PV module can be seen in [27]. A sensor for measuring the irradiance  $G$  [ $\text{W/m}^2$ ] on the plane of the solar module is connected to the measurement system (see the technical information in [28]). In addition, a temperature probe [29] is also attached on the module back surface to measure the cell temperature  $T$  [ $^{\circ}\text{C}$ ].

The measurement system, provided by biologic manufacturer [30], is composed of a EIS analyzer (SP-200) able to perform EIS analysis from  $10 \mu\text{Hz}$  up to  $7 \text{ MHz}$  interfaced with a booster (HCV-3048) supplying up to 30 A at a voltage of 48 V.

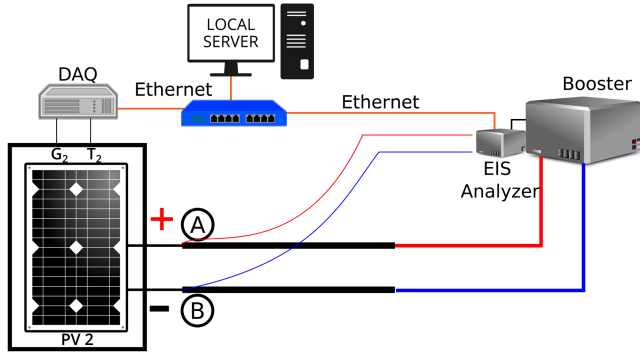


Fig. 1. Hardware setup arranged for the experimental process.

A DAQ system monitors the environmental variables and saves them in a database placed on a local server with a sampling frequency of 1 s. Additionally, the EIS analyzer is connected to the local server through an Ethernet communication for controlling the test and saving the data.

It is worth to note that, although the EIS equipment is a laboratory testing system, the proposed configuration performs an impedance analysis in a real scenario. First, using an outdoor experimental platform for providing the EIS spectrum under noncontrolled environmental conditions (irradiance and temperature) that a solar panel could find in a real PV systems. Second, utilizing low-cost sensors for acquiring the data. Naturally, for arriving to the on-board implementation of the EIS technique the lab equipment must be replaced with another hardware implementation.

Currently, different works have demonstrated that the EIS technique can be carried out using the same dc-dc converter present in standard PV installations [31]–[33]. Thus, the spotlight of this research work is not focused on hardware development. On the contrary, it seeks to exploit the EIS analysis for diagnosis purposes and degradation effects in real systems at the PV panel level working in real-outdoor conditions.

### B. PV Modeling by Using Impedance Spectra

Impedance spectroscopy allows the characterization of the electrical properties of a system in the frequency domain [34], [35]. This method injects a small-signal perturbation with a variable frequency superimposed to the system operating point. Although a PV device is not a linear system, with a small perturbation amplitude, a linear behavior can be assumed. Thus, the EIS technique should be not invasive and applicable online during the normal operation of the PV system under test. Equation (1) expresses the way of calculating and representing the impedance values as reply to the signal stimulus [34], [36]

$$Z(\omega) = \frac{V(\omega)}{I(\omega)} = \frac{\mathcal{L}\{v(t)\}}{\mathcal{L}\{i(t)\}} = \frac{V_0}{I_0} \cdot e^{-j\theta} = |Z(\omega)| \cdot e^{-j\theta}. \quad (1)$$

The frequency range and the amplitude of the small signal are the main parameters to configure for performing the EIS methodology. As shown in Table I, previous works have fixed these values from 0.01 Hz to 100 kHz for the frequency and

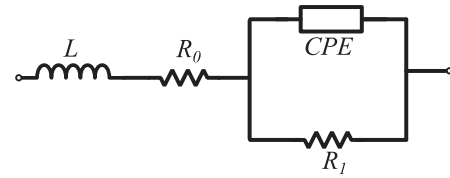


Fig. 2. Dynamic model with a CPE.

usually 100 mV value is used for the voltage amplitude [13], [23], [32]. In this article, the frequency range was fixed from 10 Hz to 50 kHz because the PV module under test responds successfully in this range.

As concerns the PV dynamic modeling, Table I shows that a high number of previous studies provide some RC electrical models able to fit in a good way the impedance values obtained for PV devices [13], [14], [37], [38]. In general, EIS spectra do not exhibit a perfect semicircle due to nonideal capacitances [14], [37], [39]. Therefore, the use of the constant phase element (CPE), especially for Si-based technologies, helps us to adjust some deviations of internal processes leading to modeling the experimental impedance data using the circuit of Fig. 2, which is described by (2). Moreover, for the frequency range adopted in this article, the ac model of a module is the same as for a single cell [14], [21]

$$Z_{eq}(\omega) = j\omega L + R_0 + \frac{R_1}{[(j\omega)^\beta Q R_1 + 1]}. \quad (2)$$

The impedance of the CPE has a particular interpretation. The  $\beta$  element can have values from 0 to 1. If  $\beta$  tends to 1, CPE is a pure capacitance. If  $\beta$  tends to 0, CPE is a pure resistor. From [40], the value of capacitor can be calculated using the components of the CPE, as shown in the following equation:

$$C = Q \left[ \frac{1}{\beta} \right] R_1 \left[ \frac{1}{\beta-1} \right]. \quad (3)$$

According to [32], the elements of the dynamic model in Fig. 2 can be associated with a solar panel since  $R_0$  represents the series ohmic losses,  $R_1$  represents the junction resistance, and  $C$  represents the junction capacitance (composed of a transition  $C_t$  capacitance and a diffusion  $C_d$  capacitance).

Fig. 3 shows the measured impedance of the PV panel under test in the complex plane and through the Bode diagram. Some basic characteristics can be straightforward associated to the circuit in Fig. 2. At low frequency ( $\omega \rightarrow 0$ ), the impedance value is given by the sum of the series ohmic losses and the junction resistance. At high frequency, the impedance value cross the  $x$ -axis and goes down almost vertically indicating that the inductive effect is dominating. This is also evident in the Bode diagram of Fig. 3 where, at high frequency, a  $180^\circ$  of phase change can be justified only by an inductive effect. Indeed, the measured impedance, acquired with the setup of Fig. 1, shows an almost straight line at high frequency, as highlighted by the dashed vertical asymptote in Fig. 3(a) indicating the presence of an inductive effect, mainly due to the cables and connectors used for the experimental setup.

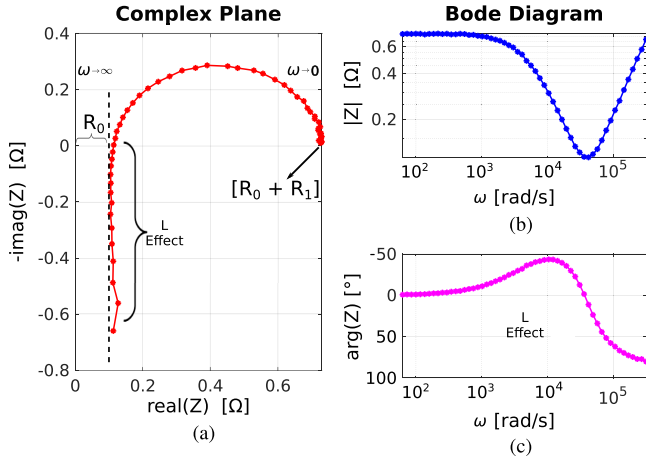


Fig. 3. (a) Complex plane. (b) Bode magnitude diagram. (c) Bode phase diagram of the impedance values of the PV panel.

The asymptote is described by the equation  $Z(\omega) = R_0 + j\omega L$ , which is the vertical boundary for the impedance spectrum in the complex plane. The variation of  $L$  affects the resonance frequency that is the frequency where the impedance spectrum crosses the real axis close to the asymptote. **The resistance  $R_0$ , since it is not depending on the frequency, only produces an horizontal translation of the impedance spectrum without modifying its shape.**

For the stimulation frequency range employed in the measurement setup, the solar cells introduce mainly a capacitive effect due to their internal p–n junctions. They exhibit inductive behavior for stimulation frequencies beyond 1 MHz, as indicated in [41].

To confirm that the inductive effect visible in the impedance spectra of Fig. 3 is dominated by parasitic effects, the measurement setup has been tested on a set of calibrated resistors within the same frequency range used for the PV measurements and at the same testing conditions. The same inductive effect was measured in each test with no significant error in the estimation of the calibrated resistors. **These tests corroborate that the inductive effect is mainly due to the MC4 connectors** used in commercial PV applications. Indeed, authors in [16], [19], and [25] also reaffirm the presence of inductive parasitic effects generated by PV connectors and wires, which is visible at the highest frequencies of the frequency stimulation range. Although the estimated inductance  $L$  is not directly related to the solar cells, it is a further parameter that can be monitored for detecting degradation in the cabling of PV panels. It is also worth to note that such parasitic effect does not appear in laboratory setup where the measurement equipment is directly connected to the PV cells by using short cables.

### C. Selection of the Operating Point for Measuring Stable EIS Spectra

During the outdoor EIS measurements, the environmental conditions are not controlled, thus, some preliminary analysis are performed for discarding noisy spectra. EIS measurements

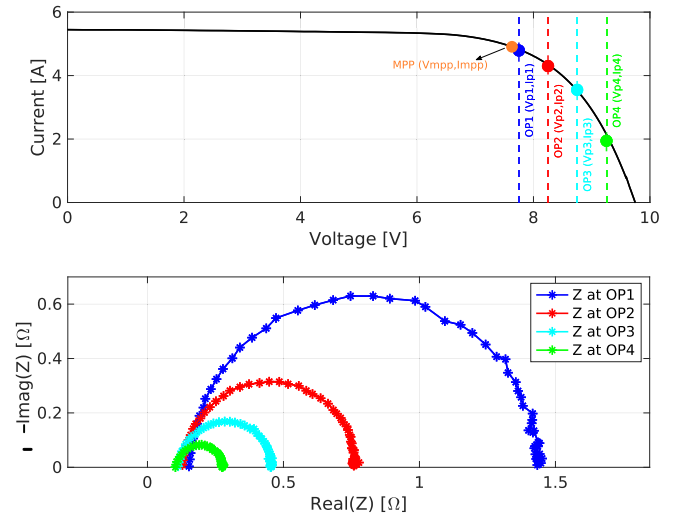


Fig. 4. Relationship between the  $I$ - $V$  curve and the impedance values in the complex plane with different operating points at a particular environmental condition ( $G = 951 \text{ W/m}^2$  and  $T = 52^\circ \text{C}$ ).

are considered reliable if were acquired in stable environmental conditions. This is checked by verifying that current and voltage are confined in a small range of variation during the EIS test, nevertheless the PV operating point could be different for each EIS test. Additionally, the well-known Kramers–Kronig test was used for validating the quality of the experimental impedance measurements [34], [37], [42]. The “Lin-KK tool” is a tool that allows applying the Kramers–Kronig test to the experimental data for validating its integrity [43], [44]. It helped us to verify the quality of all the measured impedance spectra of this article.

Fig. 4 shows four PV panel operating points of the  $I$ - $V$  curve (upper plot) where the EIS methodology is applied and their respective impedance spectra are measured (lower plot). The inductive effect, as shown in Fig. 3, is not plotted for a better visualization of impedance semiarcs appearing in the first quadrant of the complex plane. In these tests, the reduction in the real and imaginary parts visible in the impedance spectra is only related to the operating point changes from  $V_{\text{mpp}}$  to the  $V_{\text{oc}}$ . In fact, Kumar et al. [45] demonstrate **that increments in the polarization voltage increase the junction capacitance and decrease the cell dynamic resistance.** The cell dynamic resistance decrement is evident in the measurements close to zero frequencies ( $\omega \approx 0$ ), while the increment in the junction capacitance produces smaller impedance values due to the equivalent impedance of the capacitance ( $Z_c = 1/j\omega C$ ).

The obtained impedance spectra are not comparable among them since the working conditions affect significantly the parameters of the PV dynamic model [37]. In [42], a study performed in perovskite solar cells showed the same trend, reaching huge impedance values when the system was setting very close to the  $I_{\text{sc}}$ .

In Fig. 4, no EIS spectrum was measured at the left side of the MPP point because at outdoors is almost impossible to have a perfectly constant irradiance condition and, as a consequence, a clean EIS measurement in the left part of the  $I$ - $V$  curve. Here,



the current is almost independent on the voltage and strongly sensible to the irradiance, thus, EIS will provide noisy spectra not useful for diagnostic purposes.

The choice of the operating point is the first issue that must be solved when the EIS technique is applied for outdoor measurements instead of lab test.

In [42], an analysis concerning the relationship between solar cell operating points and the EIS methodology is carried out. It concludes that the open-circuit voltage ( $V_{oc}$ ) is the most suitable point because it fulfills the best conditions in terms of linearity and stability. Although the  $V_{oc}$  is the most recommended operating point for assessing the EIS methodology, it is not convenient in practical applications where PV panels are usually connected to power electronics for performing the maximum power point tracker (MPPT) algorithm that allows us to maximize the power production. Therefore, useless modifications of its working conditions are not justified since the system could have power and money losses when it goes far from the MPP state. Regarding the MPP, it is stated that it is the most interesting but challenging point due to the high sensibility of the impedance spectra with respect to the operating point. Indeed, by comparing the impedance spectra in OP1 and OP2 of Fig. 4, there is a significant change in the impedance response over a small variation of the operating point. From a diagnostic point of view, the exact knowledge of the EIS operating point is fundamental for distinguishing the variations in the impedance parameters due to the PV degradation phenomena with respect to the intrinsic variation caused by the environmental conditions or to the changes in the operating point.

In this sense, the MPP is the best choice since in normal operation of the PV systems the voltage and current are constantly measured and the MPPT algorithm operates for staying continuously close to the  $V_{mpp}$  and  $I_{mpp}$  values. Moreover, MPP is the only point that benefits of the property that the differential resistance ( $\partial V/\partial I$ ), which in the static PV small signal model, is equal to the ratio  $R_{mpp} = V_{mpp}/I_{mpp}$ . This property is a direct consequence of the maximum power condition  $\partial P/\partial V = 0$  that is valid only in MPP. In whichever other operating point, the differential resistance is a complicated expression derived by the SDM equation. More details on the PV panel differential resistance can be found in [46].

The MPP property can be exploited to verify if the EIS spectra is effectively measured in that operating point. Indeed, under the assumption that the impedance value, associated to the PV dynamic model of Fig. 2 and calculated at zero frequency ( $Z_{eq}(0)$ ), must converge to the differential resistance  $R_{mpp}$ , the following condition must be fulfilled:

$$Z_{eq}(0) = R_0 + R_1 \simeq R_{mpp} = \frac{V_{mpp}}{I_{mpp}}. \quad (4)$$

In this article, it will be verified that the previous test allows us to validate that different spectra, acquired along the time, are always associated to the MPP operating point. The choice of the operating point is also linked to the configuration of the perturbation signal. According to [37], a rule for fixing the amplitude of the small input signal is 1%–2% of the  $V_{bias}$ . In

this work, taking into account that  $V_{bias}$  corresponds to the  $V_{mpp}$ , 100 mV was established for performing the EIS analysis.

### III. EXPERIMENTAL RESULTS

#### A. System Configuration

For analyzing the degradation effects caused for variations in the series resistance, an external resistor of  $\Delta R = 0.175 \Omega$  was connected to the PV module terminals. This value has been chosen as a testing case because it produces a PV power loss of about 8% at high irradiance ( $G \geq 750 \text{ W/m}^2$ ), thus, might be assumed, for the module under test, as a reference value for considering the PV module in a degraded condition. The experimental EIS spectra obtained by the PV module at nominal conditions (without the external resistor) against the EIS measurements with the external resistance was analyzed and fitted with the PV dynamic model for detecting the  $\Delta R$  value.

Just before every EIS measurement, an  $I$ – $V$  curve measurement is acquired. This is used for settling the EIS system to operate at MPP. Additionally, the experimental  $I$ – $V$  curve allows us to identify the parameters of the classical SDM and, in particular, the series resistance value ( $R_s$ ) that is used as reference for comparing the resistance variation obtained with the EIS analysis.

#### B. Analysis of Experimental Data

Tables II and III show the parameters of the dynamic model of Fig. 2 found by using a fitting procedure. The first column is the identifier of every test. For each testing condition, the confidence intervals of the parameters (expressed as a percentage of variation with respect to the nominal value) are relatively low by assuring a well fitted model. Table II presents the parameters values at nominal conditions whereas Table III represents the parameters values with the additional external resistance  $\Delta R$ . The information regarding the environmental conditions, the MPP coordinates and  $R_s$  estimated by fitting the  $I$ – $V$  curve with the SDM are also listed in the tables.

By comparing the estimated inductance in the two testing conditions is easy to justify the increase of  $L$  in presence of the external resistance. Indeed, the  $\Delta R$  is connected to the commercial PV module through a further MC4 connector that is in series to the system under test, thus, by increasing the parasitic inductive effect.

For confirming that the EIS spectra have been really performed at MPP, the condition expressed in (4) is evaluated by using the values reported in Tables II and III. Fig. 5 shows the  $R_{mpp}$  values calculated by using the experimental ( $V_{mpp}$ ,  $I_{mpp}$ ) data (red points). Blue markers are the values of the dynamic CPE model calculated at zero frequency  $Z_{eq}(0) = R_0 + R_1$ .

The percentage error among  $R_{mpp}$  and  $Z_{eq}(0)$  for the medium and high irradiance is very small, less than 2% for both nominal condition and in presence of  $\Delta R$ . At low irradiance, as visible in Fig. 5, the maximum percentage error is, respectively, 11.5% for the nominal condition and 8.4% with  $\Delta R$ . This discrepancy is justified by the difficulty of finding exactly the MPP at low

TABLE II  
PARAMETER ESTIMATION BY USING THE CPE MODEL AT MPP UNDER DIFFERENT IRRADIANCE LEVELS

Environmental data			EIS (dynamic model)						I-V curve data		
#	$G$ [W/m <sup>2</sup> ]	$T$ [°C]	$L$ [H] $\pm$ CI[%]	$R_0$ [ $\Omega$ ] $\pm$ CI[%]	$R_1$ [ $\Omega$ ] $\pm$ CI[%]	$Q$ $\pm$ CI[%]	$\beta$ $\pm$ CI[%]	$C_{eq}$ [F]	$V_{mpp}$ [V]	$I_{mpp}$ [V]	$R_s$ [ $\Omega$ ] $\pm$ CI[%]
1	245	23.2	2.19E-06 $\pm$ 1.7	0.270 $\pm$ 4.2	10.917 $\pm$ 1.1	4.04E-05 $\pm$ 5.8	0.955 $\pm$ 0.7	2.80E-05	8.669	0.840	0.305 $\pm$ 10.2
2	286	23.4	2.28E-06 $\pm$ 2.2	0.232 $\pm$ 7.5	9.149 $\pm$ 3.3	6.59E-05 $\pm$ 11.8	0.913 $\pm$ 1.3	3.26E-05	8.783	1.044	0.258 $\pm$ 9.5
3	348	25.2	2.23E-06 $\pm$ 1.7	0.200 $\pm$ 13.7	6.481 $\pm$ 3.6	7.77E-05 $\pm$ 15.4	0.934 $\pm$ 1.7	4.55E-05	8.784	1.422	0.217 $\pm$ 6.5
4	400	25.6	2.12E-06 $\pm$ 3.8	0.188 $\pm$ 5.8	4.956 $\pm$ 1.7	9.73E-05 $\pm$ 12.6	0.939 $\pm$ 1.4	5.90E-05	8.778	1.724	0.175 $\pm$ 7.1
5	448	28.9	2.13E-06 $\pm$ 2.2	0.169 $\pm$ 2.8	3.823 $\pm$ 1.2	1.19E-04 $\pm$ 8.6	0.948 $\pm$ 1.0	7.84E-05	8.660	2.176	0.133 $\pm$ 6.0
6	482	28.7	2.17E-06 $\pm$ 2.8	0.166 $\pm$ 2.3	3.337 $\pm$ 0.9	1.31E-04 $\pm$ 6.3	0.949 $\pm$ 0.7	8.61E-05	8.602	2.435	0.146 $\pm$ 6.2
7	535	30.7	2.16E-06 $\pm$ 2.4	0.168 $\pm$ 2.4	3.025 $\pm$ 1.2	1.79E-04 $\pm$ 6.8	0.902 $\pm$ 0.8	7.95E-05	8.472	2.705	0.108 $\pm$ 5.6
8	599	33.6	2.01E-06 $\pm$ 2.8	0.154 $\pm$ 9.9	2.766 $\pm$ 2.1	3.86E-04 $\pm$ 16.7	0.817 $\pm$ 2.1	8.35E-05	8.385	3.022	0.070 $\pm$ 5.7
9	631	33.8	2.02E-06 $\pm$ 2.7	0.154 $\pm$ 8.7	2.613 $\pm$ 2.8	3.64E-04 $\pm$ 17.2	0.835 $\pm$ 2.1	9.18E-05	8.351	3.163	0.071 $\pm$ 4.2
10	754	34.2	2.04E-06 $\pm$ 2.5	0.148 $\pm$ 5.5	2.065 $\pm$ 1.9	3.68E-04 $\pm$ 19.0	0.852 $\pm$ 2.3	1.06E-04	8.364	3.863	0.055 $\pm$ 4.5
11	878	37.2	1.84E-06 $\pm$ 2.3	0.145 $\pm$ 1.7	1.679 $\pm$ 1.7	2.34E-04 $\pm$ 8.6	0.935 $\pm$ 1.1	1.36E-04	8.272	4.502	0.050 $\pm$ 3.0
12	908	42.3	2.10E-06 $\pm$ 2.3	0.143 $\pm$ 2.0	1.657 $\pm$ 1.7	1.93E-04 $\pm$ 10.8	0.973 $\pm$ 1.3	1.55E-04	8.143	4.794	0.046 $\pm$ 3.3

TABLE III  
PARAMETER ESTIMATION BY USING THE CPE MODEL AT MPP UNDER DIFFERENT IRRADIANCE LEVELS WITH AN ADDITIONAL EXTERNAL RESISTOR

Environmental data			EIS (dynamic model)						I-V curve data		
#	$G$ [W/m <sup>2</sup> ]	$T$ [°C]	$L$ [H] $\pm$ CI[%]	$R_0$ [ $\Omega$ ] $\pm$ CI[%]	$R_1$ [ $\Omega$ ] $\pm$ CI[%]	$Q$ $\pm$ CI[%]	$\beta$ $\pm$ CI[%]	$C_{eq}$ [F]	$V_{mpp}$ [V]	$I_{mpp}$ [V]	$R_s$ [ $\Omega$ ] $\pm$ CI[%]
1	250	22.4	3.61E-06 $\pm$ 1.7	0.456 $\pm$ 4.7	9.940 $\pm$ 5.1	4.43E-05 $\pm$ 14.1	0.949 $\pm$ 1.4	2.93E-05	8.505	0.853	0.479 $\pm$ 4.4
2	334	25.4	3.57E-06 $\pm$ 1.3	0.396 $\pm$ 3.3	6.012 $\pm$ 1.0	6.79E-05 $\pm$ 6.0	0.966 $\pm$ 0.7	5.18E-05	8.421	1.344	0.381 $\pm$ 3.4
3	420	27.5	3.58E-06 $\pm$ 1.0	0.365 $\pm$ 1.4	4.172 $\pm$ 1.0	9.34E-05 $\pm$ 5.8	0.968 $\pm$ 0.6	7.20E-05	8.315	1.877	0.326 $\pm$ 2.6
4	520	30.3	3.28E-06 $\pm$ 5.9	0.343 $\pm$ 3.8	2.975 $\pm$ 1.5	1.42E-04 $\pm$ 10.6	0.960 $\pm$ 1.4	1.02E-04	8.182	2.511	0.297 $\pm$ 2.0
5	650	30.5	3.30E-06 $\pm$ 1.1	0.330 $\pm$ 1.5	2.232 $\pm$ 1.1	1.84E-04 $\pm$ 7.7	0.958 $\pm$ 0.9	1.31E-04	8.037	3.267	0.269 $\pm$ 1.9
6	755	34.6	3.39E-06 $\pm$ 2.8	0.325 $\pm$ 1.8	1.867 $\pm$ 1.2	2.30E-04 $\pm$ 8.8	0.953 $\pm$ 1.0	1.57E-04	7.801	3.860	0.252 $\pm$ 1.2
7	828	39.7	3.36E-06 $\pm$ 3.3	0.317 $\pm$ 2.3	1.583 $\pm$ 1.8	2.81E-04 $\pm$ 13.5	0.943 $\pm$ 1.8	1.77E-04	7.616	4.220	0.248 $\pm$ 1.0
8	886	35.6	3.35E-06 $\pm$ 3.6	0.319 $\pm$ 2.3	1.416 $\pm$ 1.5	2.38E-04 $\pm$ 13.2	0.968 $\pm$ 1.7	1.83E-04	7.676	4.487	0.242 $\pm$ 0.8
9	975	38.6	3.24E-06 $\pm$ 4.6	0.318 $\pm$ 1.8	1.259 $\pm$ 1.1	3.11E-04 $\pm$ 13.4	0.949 $\pm$ 1.9	2.04E-04	7.517	4.836	0.229 $\pm$ 0.4
10	1028	38.5	3.17E-06 $\pm$ 5.6	0.318 $\pm$ 1.9	1.219 $\pm$ 1.5	2.71E-04 $\pm$ 15.2	0.969 $\pm$ 1.7	2.10E-04	7.487	5.084	0.231 $\pm$ 0.6

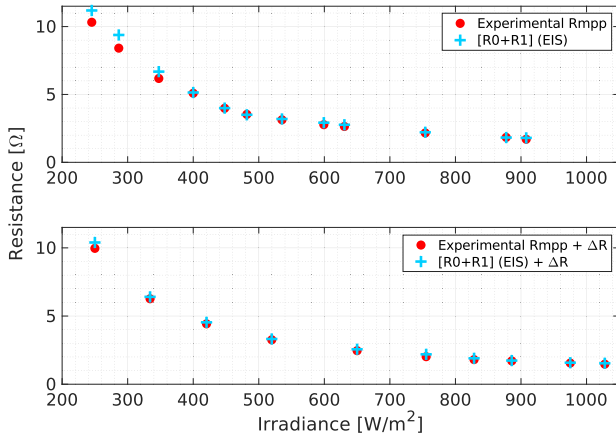


Fig. 5. Comparison of the experimental  $R_{mpp}$  values and the impedance at zero frequency using the CPE model. Upper plot: PV module at nominal conditions. Lower plot: PV module with the external resistor.

irradiance because the power versus voltage curve is flat around the MPP and, due to the finite resolution of the measurement system, small differences can be introduced in settling the operating point during the EIS. If the error at low irradiance is considered unacceptable such measure should be discarded. In the following, all the measurements shown in Fig. 5 are assumed to be valid, thus, the dynamic CPE model is considered properly tuned for describing the behavior of the PV module at MPP for both cases, nominal condition, and with the additional resistance in the full range of the environmental conditions. It is worth to note that the data required to perform this test are only the EIS spectra and the measured voltage and current, thus it is suitable

for the on-board execution giving the possibility to guarantee the coherence of the experimental EIS data with the MPP operation with a simple check.

### C. Identification of the Series Resistance Degradation

Fig. 6 graphically illustrates the effect of series resistance degradation in the  $I-V$  curves (upper plot) and the impedance values measured with the EIS methodology (lower plot) in the same environmental conditions. It is well-known that an increase in the series resistance impacts on the slope of the  $I-V$  curve in proximity of  $V_{oc}$ , which is reflected on a displacement of the MPP. Differently, the impact of the series resistance variation produces an horizontal translation on the impedance spectra that is visible at high frequency and mainly affects the  $R_0$  value. Therefore, the identification of the series resistance degradation by using the  $I-V$  curves requires to measure voltage and current around  $V_{oc}$  for calculating the slope of the  $I-V$  curves and then estimates the  $R_s$  variation. On the contrary, the EIS methodology requires only to estimate the parameters of the PV dynamic model by using the impedance spectra measured at MPP and then approximate the series resistance degradation through the  $R_0$  parameter variation.

A further experimental campaign has been carried out on the PV panel under test by performing the impedance measurement in different points of the right part of the  $I-V$  curve. Both healthy (nominal) and degraded conditions were analyzed. Fig. 7 shows the values of the CPE dynamic model parameters for the PV panel operating in healthy and degraded condition for different operating points spreading from  $V_{oc}$  up to the left of MPP.

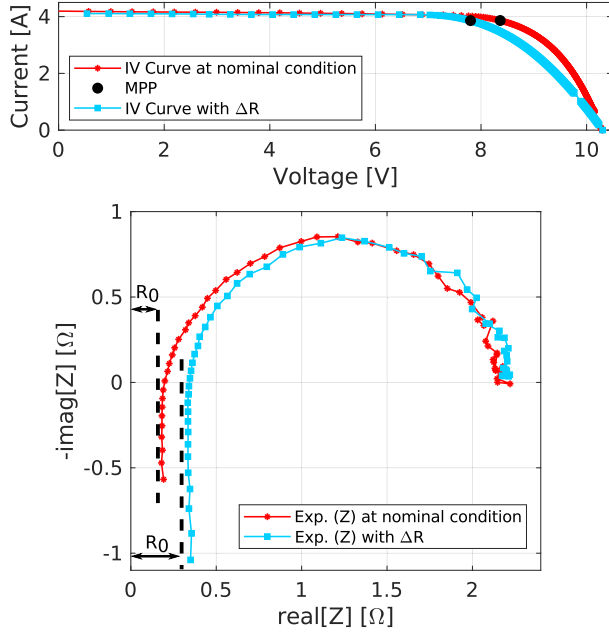


Fig. 6. Comparison of test cases #10 (red markers) and #6 (blue markers) from Tables II and III, respectively.

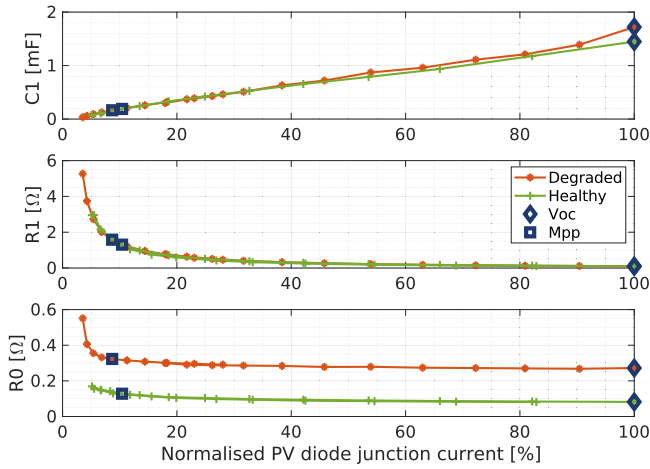


Fig. 7. Parameters variation of the CPE dynamic model as function of the operating point of the  $I$ - $V$  curve.

It is worth to note that the additional series resistance change the slope of the  $I$ - $V$  curve by making not comparable the impedance spectra for the same testing point when the panel operates in healthy or emulated degraded condition, for this reason, the parameters have been plotted as function of the normalized current flowing in the p-n junction. The latter is calculated as the difference between the short-circuit current and the current delivered by the PV panel for each point of the  $I$ - $V$  curve where the impedance spectrum has been measured.

The graphs clearly show how the additional resistance only impact on the  $R_0$  parameter how already confirmed by the analysis performed only in the MPP point.

For forward biased solar cells, the capacitive effect is dominated by the diffusion capacitance [47], which is linear with

TABLE IV  
PRELIMINARY COMPARISON OF THE SERIES RESISTANCE VARIATION FOUND BY THE SDM AND THE DYNAMIC CPE MODEL

Additional resistance				Nominal case				Variation			
$G$ [W/m <sup>2</sup> ]	$T$ [°C]	$R_s$ [Ω]	$R_0$ [Ω]	$G$ [W/m <sup>2</sup> ]	$T$ [°C]	$R_s$ [Ω]	$R_0$ [Ω]	$\Delta R_s$ [Ω]	$\Delta R_0$ [Ω]		
250	22.4	0.479	0.456	245	23.2	0.305	0.270	0.174	0.186		
520	30.3	0.297	0.343	535	30.7	0.108	0.168	0.189	0.175		
886	35.6	0.242	0.319	878	37.2	0.050	0.145	0.192	0.174		

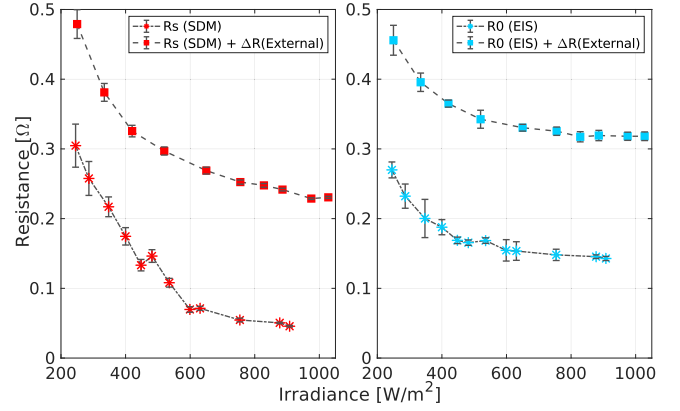


Fig. 8. Left plot:  $R_s$  estimated by using SDM. Right plot:  $R_0$  estimated by using EIS spectra. The asterisks refer to the parameters in nominal conditions. The square markers refer to the tests with the external resistance.

respect to the current flowing in the p-n junction, as confirmed by  $C_1$  plot in Fig. 7. As concerns the resistive effect of the p-n junction, which is described by the  $R_1$  parameter, the plot of Fig. 7 clearly put into evidence that its variation is much more pronounced around the MPP, thus, it is expected that it could be a further indicator for detecting other degradation phenomena when the solar cells operate in MPP.

Table IV shows a comparison of the series resistance for the cases with and without the external resistor having similar irradiance and temperature conditions. These three values gives a preliminary analysis at low, medium, and high irradiance levels. The change expressed by the dynamic CPE model in its  $R_0$  parameter shows a better estimation of the true additional resistance ( $\Delta R = 0.175$  Ω).

Fig. 8 shows the trend of the series resistance parameters  $R_s$  and  $R_0$  evaluated by fitting the static model (SDM) and the dynamic model (CPE model), respectively, with the  $I$ - $V$  curves and the EIS spectra in the different environmental conditions reported in Tables II and III. All the values display the confidence interval given by the fitting procedure. Despite the resistance values obtained from the static (SDM) and dynamic models cannot be directly compared because derived from different experimental data, both recognize a similar degraded effect introduced by the external series resistance. The difference in the series resistance estimation is also justified by the fact that the two models describe different characteristics of the PV module. Indeed the SDM reproduces the static nonlinear behavior and its  $I$ - $V$  profile using some nonlinear elements as a diode. In contrast, the CPE model is a dynamic small signal model used for representing the dynamic response of the PV module at a specific operating point, thus, the meaning of  $R_s$  and  $R_0$  is not

TABLE V  
PARAMETERS OF THE REGRESSION CURVES FOR THE SERIES RESISTANCE  
VALUES FOUND USING THE SDM AND THE DYNAMIC MODEL (EIS)

Model	Regression	Parameters	
		a	b
Static model (SDM)	Regression 1	-0.066	93.040
	Regression 2	0.147	80.374
Dynamic model (EIS)	Regression 3	0.090	40.774
	Regression 4	0.266	44.975

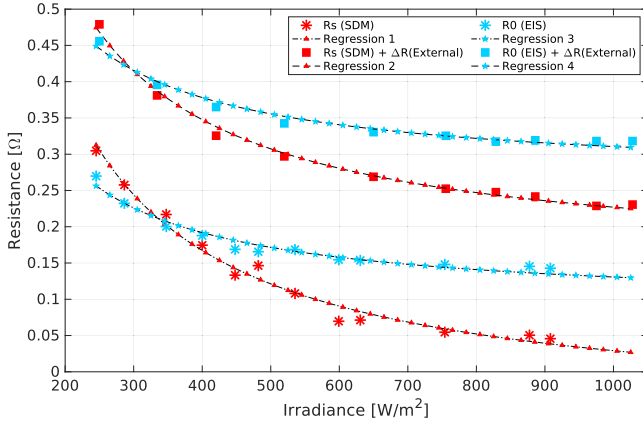


Fig. 9. Regression process for the values calculated using the SDM and the dynamic model in the two test cases.

exactly the same, nevertheless both refer to the ohmic losses and then exploitable for detecting degradation phenomena in the PV module.

A comparison by using all the experimental cases reported in Tables II and III has been done by introducing a regression curve for describing the parameters ( $R_s$ ) and ( $R_0$ ) as function of the irradiance. Equation (5) shows the general expression that best fits the experimental data. It is worth to note that the actual outdoor experimental campaign is referring to a short period (few weeks) that did not allow us to cover a wide combination of different irradiance and temperature conditions. Indeed the outdoor environmental conditions are strictly correlated during the days of the same season and only by considering long testing period it is possible to have an experimental campaign covering a large range of temperature (e.g., by considering summer and winter period). For this reason, the temperature variation encountered in the actual experimental tests has been considered having a negligible impact on the series resistance estimation and not accounted in the regression function as an additional predictor. Table V shows the parameter values of the regression curves describing the series resistance found by the static (SDM) and dynamic (CPE) models

$$R = a + \left( \frac{b}{G} \right). \quad (5)$$

Fig. 9 displays the resistance values of the models for every irradiance level. The regression curves modeled using the SDM show two not-aligned tendencies that generate unbalanced approximations for the series resistance variations, especially at low irradiance. In contrast, the regression curves calculated

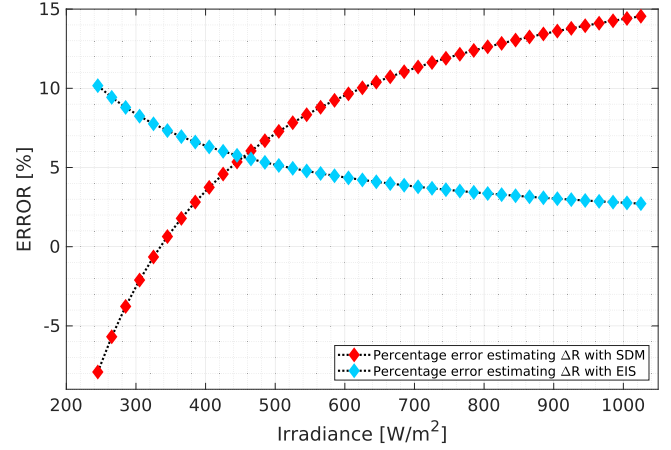


Fig. 10. Percentage error estimation between the nominal delta value ( $\Delta R = 0.175 \Omega$ ) and the value given by the SDM and the dynamic model using the regression curves for the whole irradiance range.

TABLE VI  
PRELIMINARY COMPARISON OF THE SERIES RESISTANCE VARIATION FOUND BY  
THE SDM AND THE CPE MODEL ( $\Delta R = 0.35 \Omega$ )

Additional resistance				Nominal case				Variation	
$G$ [W/m²]	$T$ [°C]	$R_s$ [Ω]	$R_0$ [Ω]	$G$ [W/m²]	$T$ [°C]	$R_s$ [Ω]	$R_0$ [Ω]	$\Delta R_s$ [Ω]	$\Delta R_0$ [Ω]
297	29.2	0.481	0.541	286	23.4	0.258	0.232	0.223	0.309
361	27.2	0.446	0.529	347	25.2	0.217	0.200	0.229	0.329
414	27.5	0.435	0.537	400	25.6	0.175	0.188	0.260	0.349
479	29.6	0.425	0.516	482	28.7	0.146	0.166	0.279	0.350
542	31.4	0.402	0.504	535	30.7	0.108	0.168	0.294	0.336
596	34.3	0.402	0.496	599	33.6	0.070	0.154	0.332	0.342

with the dynamic CPE model show a more uniform difference throughout the whole irradiance range. It indicates a more stable and reliable approximation of the series resistance variation at all irradiance levels.

In fact, the error between the physical resistance value and each estimation (see Fig. 10) shows that the dynamic (CPE) model approximates in a good way the resistance variation ( $\Delta R$ ), even better than the static model (SDM), especially in the range from medium to high irradiance. The dynamic (CPE) model also shows a positive attribute since it displays an estimated error always positive (overestimation) and tends to stabilize from low to high irradiance levels. In contrast, the SDM depicts under and overestimations from low to high irradiance. This behavior reveals a technical weakness and supports the idea that the dynamic (CPE) model is most reliable for approximating the series resistance variations in all irradiance levels. As an additional test, the external resistance is changed to  $\Delta R = 0.35 \Omega$ . Table VI compares some similar irradiance values and corroborates the results previously discussed. Although the available data only covers from low to medium irradiance range, it again shows that the dynamic (CPE) model, calculated by using the EIS methodology, estimates the degradation of series resistance better than the SDM.

#### IV. CONCLUSION

The obtained outcomes have illustrated the high potential EIS methodology has for real-time monitoring conditions. The



EIS-based diagnostic method can be fruitfully employed in PV systems working at MPP in outdoor conditions without altering the standard operation of the system. Therefore, it avoids power losses and undesirable changing in the PV system operation. The dynamic model built with the impedance measurements provided better approximations than the classic static model (SDM) for a specific degradation process, such as series resistance variations.

This work is the first attempt to apply the EIS methodology for detecting the PV degradation phenomena in real-operative outdoor conditions. The validation of experimental results demonstrated the potentiality of the proposed approach to detect other PV degradation phenomena as well as by-pass diode failure, partial shading conditions, and hot-spot detection that usually happen in PV sources operating in outdoor conditions.

## REFERENCES

- [1] B. Uzum, A. Onen, H. M. Hasanien, and S. M. Mueen, "Rooftop solar PV penetration impacts on distribution network and further growth factors—A comprehensive review," *Electronics*, vol. 10, no. 1, pp. 1–31, 2021, doi: [10.3390/electronics10010055](https://doi.org/10.3390/electronics10010055).
- [2] M. Aghaei et al., "Review of degradation and failure phenomena in photovoltaic modules," *Renewable Sustain. Energy*, vol. 159, 2022, Art. no. 112160, doi: [10.1016/j.rser.2022.112160](https://doi.org/10.1016/j.rser.2022.112160).
- [3] T. S. Ustun, Y. Nakamura, J. Hashimoto, and K. Otani, "Performance analysis of PV panels based on different technologies after two years of outdoor exposure in Fukushima, Japan," *Renewable Energy*, vol. 136, pp. 159–178, 2019, doi: [10.1016/j.renene.2018.12.100](https://doi.org/10.1016/j.renene.2018.12.100).
- [4] M. Zaimi, H. El Achoubi, O. Zegoudi, A. Ibral, and E. Assaid, "Numerical method and new analytical models for determining temporal changes of model-parameters to predict maximum power and efficiency of PV module operating outdoor under arbitrary conditions," *Energy Convers. Manage.*, vol. 220, 2020, Art. no. 113071, doi: [10.1016/j.enconman.2020.113071](https://doi.org/10.1016/j.enconman.2020.113071).
- [5] S. Hara, H. Douzono, M. Imamura, and T. Yoshioka, "Estimation of photovoltaic cell parameters using measurement data of photovoltaic module string currents and voltages," *IEEE J. Photovolt.*, vol. 12, no. 2, pp. 540–545, Mar. 2022, doi: [10.1109/JPHOTOV.2021.3135262](https://doi.org/10.1109/JPHOTOV.2021.3135262).
- [6] M. Piliouguine et al., "Parameters extraction of single diode model for degraded photovoltaic modules," *Renewable Energy*, vol. 164, pp. 674–686, 2021, doi: [10.1016/j.renene.2020.09.035](https://doi.org/10.1016/j.renene.2020.09.035).
- [7] D. Sera, R. Teodorescu, and P. Rodriguez, "Photovoltaic module diagnostics by series resistance monitoring and temperature and rated power estimation," in *Proc. 34th IEEE Conf. Ind. Electron.*, 2008, pp. 2195–2199, doi: [10.1109/IECON.2008.4758297](https://doi.org/10.1109/IECON.2008.4758297).
- [8] D. Sera and R. Teodorescu, "Robust series resistance estimation for diagnostics of photovoltaic modules," in *Proc. 35th IEEE Conf. Ind. Electron.*, 2009, pp. 800–805, doi: [10.1109/IECON.2009.5415022](https://doi.org/10.1109/IECON.2009.5415022).
- [9] J. S. Stein, S. McCaslin, C. W. Hansen, W. E. Boyson, and C. D. Robinson, "Measuring PV system series resistance without full IV curves," in *Proc. 40th IEEE Photovolt. Specialist Conf.*, 2014, pp. 2032–2036, doi: [10.1109/PVSC.2014.6925326](https://doi.org/10.1109/PVSC.2014.6925326).
- [10] M. G. Deceglie, T. J. Silverman, B. Marion, and S. R. Kurtz, "Real-time series resistance monitoring in PV systems without the need for I–V curves," *IEEE J. Photovolt.*, vol. 5, no. 6, pp. 1706–1709, Nov. 2015, doi: [10.1109/jphotov.2015.2478070](https://doi.org/10.1109/jphotov.2015.2478070).
- [11] G. Spagnuolo, K. Lappalainen, S. Valkealahti, and P. Manganiello, "Identification and diagnosis of a photovoltaic module based on outdoor measurements," in *Proc. IEEE Milan PowerTech*, 2019, pp. 1–6, doi: [10.1109/PTC.2019.8810767](https://doi.org/10.1109/PTC.2019.8810767).
- [12] Y. C. Hsieh et al., "Parameter identification of one-diode dynamic equivalent circuit model for photovoltaic panel," *IEEE J. Photovolt.*, vol. 10, no. 1, pp. 219–225, Jan. 2020, doi: [10.1109/JPHOTOV.2019.2951920](https://doi.org/10.1109/JPHOTOV.2019.2951920).
- [13] N. Katayama, S. Osawa, S. Matsumoto, T. Nakano, and M. Sugiyama, "Degradation and fault diagnosis of photovoltaic cells using impedance spectroscopy," *Sol. Energy Mater. Sol. Cells*, vol. 194, pp. 130–136, 2019, doi: [10.1016/j.solmat.2019.01.040](https://doi.org/10.1016/j.solmat.2019.01.040).
- [14] T. Yeow, J. Sun, Z. Yao, J.-N. Jaubert, and K. P. Musselman, "Evaluation of impedance spectroscopy as a tool to characterize degradation mechanisms in silicon photovoltaics," *Sol. Energy*, vol. 184, pp. 52–58, 2019, doi: [10.1016/j.solener.2019.03.088](https://doi.org/10.1016/j.solener.2019.03.088).
- [15] D. Chenvidhya, K. Kirtikara, and C. Jivacate, "A new characterization method for solar cell dynamic impedance," *Sol. Energy Mater. Sol. Cells*, vol. 80, no. 4, pp. 459–464, 2003, doi: [10.1016/j.solmat.2003.06.011](https://doi.org/10.1016/j.solmat.2003.06.011).
- [16] S. Kumar, P. Singh, and G. Chilana, "Study of silicon solar cell at different intensities of illumination and wavelengths using impedance spectroscopy," *Sol. Energy Mater. Sol. Cells*, vol. 93, no. 10, pp. 1881–1884, 2009, doi: [10.1016/j.solmat.2009.07.002](https://doi.org/10.1016/j.solmat.2009.07.002).
- [17] J. E. Garland, D. J. Crain, J. P. Zheng, C. M. Sulyma, and D. Roy, "Electro-analytical characterization of photovoltaic cells by combining voltammetry and impedance spectroscopy: Voltage dependent parameters of a silicon solar cell under controlled illumination and temperature," *Energy Environ. Sci.*, vol. 4, pp. 485–498, 2011, doi: [10.1039/C0EE00307G](https://doi.org/10.1039/C0EE00307G).
- [18] P. Yadav, K. Pandey, B. Tripathi, and M. Kumar, "Investigation of interface limited charge extraction and recombination in polycrystalline silicon solar cell: Using DC and AC characterization techniques," *Sol. Energy*, vol. 116, pp. 293–302, 2015, doi: [10.1016/j.solener.2015.04.011](https://doi.org/10.1016/j.solener.2015.04.011).
- [19] J. Panigrahi et al., "Impedance spectroscopy of crystalline silicon solar cell: Observation of negative capacitance," *Sol. Energy*, vol. 136, pp. 412–420, 2016, doi: [10.1016/j.solener.2016.06.041](https://doi.org/10.1016/j.solener.2016.06.041).
- [20] O. I. Olayiwola and P. S. Barendse, "Characterization of silicon-based photovoltaic cells using broadband impedance spectroscopy," *IEEE Trans. Ind. Appl.*, vol. 54, no. 6, pp. 6309–6319, Nov./Dec. 2018, doi: [10.1109/TIA.2018.2850025](https://doi.org/10.1109/TIA.2018.2850025).
- [21] A. Bouzidi, W. Jilani, I. Yahia, and H. Zahran, "Impedance spectroscopy of monocrystalline silicon solar cells for photosensor applications: Highly sensitive device," *Physica B*, vol. 596, 2020, Art. no. 412375, doi: [10.1016/j.physb.2020.412375](https://doi.org/10.1016/j.physb.2020.412375).
- [22] J. Johnson, D. Schoenwald, S. Kuszmaul, J. Strauch, and W. Bower, "Creating dynamic equivalent PV circuit models with impedance spectroscopy for arc fault modeling," in *Proc. 37th IEEE Photovolt. Specialists Conf.*, 2011, pp. 2328–2333, doi: [10.1109/PVSC.2011.6186419](https://doi.org/10.1109/PVSC.2011.6186419).
- [23] M. I. Oprea et al., "Detection of potential induced degradation in c-Si PV panels using electrical impedance spectroscopy," in *Proc. 43rd IEEE Photovolt. Specialists Conf.*, 2016, pp. 1575–1579, doi: [10.1109/PVSC.2016.7749885](https://doi.org/10.1109/PVSC.2016.7749885).
- [24] M. U. Saleh et al., "Detection and localization of damaged photovoltaic cells and modules using spread spectrum time domain reflectometry," *IEEE J. Photovolt.*, vol. 11, no. 1, pp. 195–201, Jan. 2021, doi: [10.1109/JPHOTOV.2020.3030185](https://doi.org/10.1109/JPHOTOV.2020.3030185).
- [25] M. U. Saleh et al., "Signal propagation through piecewise transmission lines for interpretation of reflectometry in photovoltaic systems," *IEEE J. Photovolt.*, vol. 9, no. 2, pp. 506–512, Mar. 2019, doi: [10.1109/JPHOTOV.2018.2884011](https://doi.org/10.1109/JPHOTOV.2018.2884011).
- [26] G. Kampitzi, E. Batzelis, R. van Erp, and E. Matioli, "Parallel PV configuration with magnetic-free switched capacitor module-level converters for partial shading conditions," *Energies*, vol. 14, no. 2, pp. 1–17, 2021, doi: [10.3390/en14020456](https://doi.org/10.3390/en14020456).
- [27] Solbian Flex SP50–L Flexible Photovoltaic Panels. 2022. Accessed: Apr. 26, 2022. [Online]. Available: [https://www.dropbox.com/s/xtdp3axmxqkbg2a/SOLBIAN\\_50W\\_sp50L\\_eng.pdf](https://www.dropbox.com/s/xtdp3axmxqkbg2a/SOLBIAN_50W_sp50L_eng.pdf)
- [28] LiteMeter 1-10 V Pro, 2019. Accessed: Apr. 26, 2022. [Online]. Available: <https://www.dropbox.com/s/3n7ah2ffkcnj2qb/LiteMeter.pdf>
- [29] Texas Instruments LM35 Precision Centigrade Temperature Sensors, 2017. Accessed: Apr. 26, 2022. [Online]. Available: <https://www.dropbox.com/s/93mn12yd44r3pwt/lm35.pdf>
- [30] BioLogic. Accessed: Apr. 26, 2022. [Online]. Available: <https://www.biologic.net/>
- [31] M. A. Varnosfaderani and D. Strickland, "Online electrochemical impedance spectroscopy (EIS) estimation of a solar panel," *Vacuum*, vol. 139, pp. 185–195, 2017, doi: [10.1016/j.vacuum.2017.01.011](https://doi.org/10.1016/j.vacuum.2017.01.011).
- [32] L. Shelembe and P. Barendse, "Online condition monitoring of photovoltaic (PV) cells by implementing electrical impedance spectroscopy using a switch-mode DC-DC converter," in *Proc. IEEE Energy Convers. Congr. Expo.*, 2020, pp. 2136–2141, doi: [10.1109/ecce44975.2020.9235596](https://doi.org/10.1109/ecce44975.2020.9235596).
- [33] O. I. Olayiwola and P. S. Barendse, "Power electronic implementation of electrochemical impedance spectroscopy on photovoltaic modules," in *Proc. IEEE Energy Convers. Congr. Expo.*, 2020, pp. 3654–3661, doi: [10.1109/ecce44975.2020.9236404](https://doi.org/10.1109/ecce44975.2020.9236404).
- [34] A. Lasia, *Electrochemical Impedance Spectroscopy and Its Applications*, 3rd ed. Berlin, Germany: Springer, 2014.
- [35] E. Barsoukov and J. R. Macdonald, *Impedance Spectroscopy: Theory, Experiment, and Applications*, 3rd ed. Hoboken, NJ, USA: Wiley, 2018.
- [36] P. Boškoski, *Fast Electrochemical Impedance Spectroscopy*. Berlin, Germany: Springer, 2017.

- [37] O. I. Olayiwola and P. S. Barendse, "Photovoltaic cell/module equivalent electric circuit modeling using impedance spectroscopy," *IEEE Trans. Ind. Appl.*, vol. 56, no. 2, pp. 1690–1701, Mar./Apr. 2020, doi: [10.1109/tia.2019.2958906](https://doi.org/10.1109/tia.2019.2958906).
- [38] E. V. Hauff, "Impedance spectroscopy for emerging photovoltaics," *J. Phys. Chem. C*, vol. 123, no. 18, pp. 11329–11346, 2019, doi: [10.1021/acs.jpcc.9b00892](https://doi.org/10.1021/acs.jpcc.9b00892).
- [39] S. M. Abdulrahim, Z. Ahmad, J. Bahadra, and N. J. Al-Thani, "Electrochemical impedance spectroscopy analysis of hole transporting material free mesoporous and planar perovskite solar cells," *Nanomaterials*, vol. 10, 2020, Art. no. 1635, doi: [10.3390/nano10091635](https://doi.org/10.3390/nano10091635).
- [40] A. Sacco, "Electrochemical impedance spectroscopy: Fundamentals and application in dye-sensitized solar cells," *Renewable Sustain. Energy Rev.*, vol. 79, pp. 814–829, 2017, doi: [10.1016/j.rser.2017.05.159](https://doi.org/10.1016/j.rser.2017.05.159).
- [41] K. A. Kim, C. Xu, L. Jin, and P. T. Krein, "A dynamic photovoltaic model incorporating capacitive and reverse-bias characteristics," *IEEE J. Photovolt.*, vol. 3, no. 4, pp. 1334–1341, Oct. 2013, doi: [10.1109/JPHOTOV.2013.2276483](https://doi.org/10.1109/JPHOTOV.2013.2276483).
- [42] E. V. Hauff and D. Klotz, "Impedance spectroscopy for perovskite solar cells: Characterisation, analysis, and diagnosis," *J. Mater. Chem. C*, vol. 10, pp. 742–761, 2022, doi: [10.1039/D1TC04727B](https://doi.org/10.1039/D1TC04727B).
- [43] B. A. Boukamp, "A linear Kronig-Kramers transform test for immittance data validation," *J. Electrochem. Soc.*, vol. 142, no. 6, pp. 1885–1894, 1995, doi: [10.1149/1.2044210](https://doi.org/10.1149/1.2044210).
- [44] M. Schönleber, D. Klotz, and E. Ivers-Tiffée, "A method for improving the robustness of linear Kramers-Kronig validity tests," *Electrochimica Acta*, vol. 131, pp. 20–27, 2014, doi: [10.1016/j.electacta.2014.01.034](https://doi.org/10.1016/j.electacta.2014.01.034).
- [45] R. A. Kumar, M. S. Suresh, and J. Nagaraju, "Facility to measure solar cell AC parameters using an impedance spectroscopy technique," *Rev. Sci. Instrum.*, vol. 72, pp. 3422–3426, 2001, doi: [10.1063/1.1386632](https://doi.org/10.1063/1.1386632).
- [46] N. Femia, G. Petrone, G. Spagnuolo, and M. Vitelli, *Power Electronics and Control Techniques for Maximum Energy Harvesting in Photovoltaic Systems*. Boca Raton, FL, USA: CRC Press, 2013.
- [47] K. A. Kim, G.-S. Seo, B.-H. Cho, and P. T. Krein, "Photovoltaic hot-spot detection for solar panel substrings using AC parameter characterization," *IEEE Trans. Power Elect.*, vol. 31, no. 2, pp. 1121–1130, Feb. 2016, doi: [10.1109/TPEL.2015.2417548](https://doi.org/10.1109/TPEL.2015.2417548).